

Contrasting Charge-Carrier Dynamics across Key Metal-Halide Perovskite Compositions through In Situ Simultaneous Probes

Aleksander M. Ulatowski, Karim A. Elmestekawy, Jay B. Patel, Nakita K. Noel, Siyu Yan, Hans Kraus, Peter G. Huggard, Michael B. Johnston,* and Laura M. Herz*

Metal-halide perovskites have proven to be a versatile group of semiconductors for optoelectronic applications, with ease of bandgap tuning and stability improvements enabled by halide and cation mixing. However, such compositional variations can be accompanied by significant changes in their charge-carrier transport and recombination regimes that are still not fully understood. Here, a novel combinatorial technique is presented to disentangle such dynamic processes over a wide range of temperatures, based on transient free-space, high-frequency microwave conductivity and photoluminescence measurements conducted simultaneously in situ. Such measurements are used to reveal and contrast the dominant charge-carrier recombination pathways for a range of key compositions: prototypical methylammonium lead iodide perovskite (MAPbI₃), the stable mixed formamidinium-caesium lead-halide perovskite FA_{0.83}Cs_{0.17}PbBr_{0.6}I_{2.4} targeted for photovoltaic tandems with silicon, and fully inorganic wide-bandgap CsPbBr₃ aimed toward light sources and X-ray detector applications. The changes in charge-carrier dynamics in FA_{0.83}Cs_{0.17}PbBr_{0.6}I_{2.4} across temperatures are shown to be dominated by radiative processes, while those in MAPbI₃ are governed by energetic disorder at low temperatures, low-bandgap minority-phase inclusions around the phase transition, and non-radiative processes at room temperature. In contrast, CsPbBr₃ exhibits significant charge-carrier trapping at low and high temperatures, highlighting the need for improvement of material processing techniques for wide-bandgap perovskites.

1. Introduction

The excellent optoelectronic properties of metal-halide perovskites have attracted intense interest from the scientific community over the last decade.^[1] The ease of fabrication of these materials, through solution processing and thermal evaporation, has allowed for the exploration of a large range of chemical compositions. Such stoichiometric variations have underpinned the discovery of bandgap tunability through halide and metal ion substitution^[2–5] as well as the optimization of material stability, for example, through cation alloying and additives.^[6,7] Relatively straightforward bandgap engineering makes metal-halide perovskites highly versatile for optoelectronic devices, including photovoltaic single- and multi-junction technology and light-emitting applications over a wide range of wavelengths. For photovoltaic applications, in particular, iodine-rich lead-halide perovskites are ideal for single-junction solar cells performing near the Shockley–Queisser limit,^[8] while all-perovskite multi-junction cells require both low-bandgap bottom layers offered by mixed tin-lead iodide perovskites

A. M. Ulatowski, K. A. Elmestekawy, J. B. Patel, N. K. Noel, S. Yan, H. Kraus, M. B. Johnston, L. M. Herz
Department of Physics
University of Oxford
Clarendon Laboratory, Parks Road, Oxford OX1 3PU, UK
E-mail: michael.johnston@physics.ox.ac.uk; laura.herz@physics.ox.ac.uk

P. G. Huggard
STFC RAL Space
Rutherford Appleton Laboratory
Harwell, Didcot OX11 0QX, UK
L. M. Herz
Institute for Advanced Study
Technical University of Munich
Lichtenbergstrasse 2a, D-85748 Garching, Germany

 The ORCID identification number(s) for the author(s) of this article can be found under <https://doi.org/10.1002/adfm.202305283>

© 2023 The Authors. Advanced Functional Materials published by Wiley-VCH GmbH. This is an open access article under the terms of the Creative Commons Attribution License, which permits use, distribution and reproduction in any medium, provided the original work is properly cited.

DOI: 10.1002/adfm.202305283

and wide-bandgap bromide-rich lead-halide perovskites as top layers.^[5,9] Meanwhile, top layers for perovskite-silicon two-terminal tandem solar cells should exhibit optimized performance for bandgaps near 1.75 eV,^[10,11] which could be achieved by lead mixed-halide perovskites with intermediate bromide-iodide ratios. However, these compositions unfortunately show a tendency toward phase segregation,^[12,13] and therefore the highest bromide content for which stability is still achieved ($\approx 20\%$ Br) is typically used instead.^[14,15]

While metal-halide perovskites have clearly shown great potential for such applications, the dynamic electronic processes that ultimately determine device performance are still a matter of much debate.^[16–19] Here, the phenomenal compositional space available to metal-halide perovskites has been particularly challenging, because such tuning may inadvertently affect a wide range of critical factors including defect chemistry,^[20] electron-phonon coupling,^[21,22] exciton binding energies,^[23,24] energetic disorder,^[25,26] and phase purity.^[27] Such variations have made accurate observation and modeling of charge-carrier recombination processes critical to the guidance of materials' synthesis and development. To examine such effects in metal-halide perovskites, a range of single-probe techniques have been applied successfully, including time-resolved microwave conductivity (TRMC),^[18,28–31] time-resolved photoluminescence (TRPL),^[32–35] optical-pump–THz-probe (OPTP),^[36–38] and transient-absorption (TA) measurements.^[20,39] These can provide excellent insight into the dynamics of charge-carrier recombination following photoexcitation but are limited to tracking only one property of the material (e.g., luminescence or conductivity) at a time. Such single-technique approaches thus inhibit the reliable disentanglement of the various processes involved in photoexcited charge-carrier population decay, such as charge-carrier trapping, de-trapping, dopant-mediated recombination, and band-to-band recombination. While a combination of different techniques may be applied in succession in order to obtain complementary datasets,^[20,39,40] these often suffer from being conducted under different measurement conditions, such as variations in pulsed excitation-fluence regimes, pulse repetition rates, or environmental gases (measurements under vacuum, N_2 , or in air), which have substantial effects on the observed dynamics.^[34,41–43] Combinatorial studies thus hold great promise, involving a number of different techniques applied at the same time and under the same environment and excitation conditions. These may however present a variety of technical challenges that need to be resolved.

In this study, we contrast the charge-carrier recombination dynamics across three key metal-halide perovskites through a novel approach that integrates transient microwave conductivity and photoluminescence measurements in situ. Such combined measurements have in the past been impeded by the use of microwave cavities to enhance signals, complicating the effective extraction of luminescence from the material.^[44] We here overcome this issue by employing a custom-built setup based on high-frequency microwaves channeled through free-space optics without the presence of a cavity. This approach allows us to acquire TRPL and spectrally resolved photoluminescence data at the same time and under the same excitation conditions, as well as to integrate the combined system with a standard optical cryostat allowing control of sample temperatures down to 4 K.

We show that this combinatorial experimental method, together with a unified model that simultaneously reproduces both conductivity and photoluminescence transients, yields powerful insights into the mechanisms dominating charge-carrier recombination across a range of chemical compositions of metal-halide perovskites. We examine thin films of i) the stable mixed formamidinium-caesium lead-halide perovskite $FA_{0.83}Cs_{0.17}PbBr_{0.6}I_{2.4}$ targeted for photovoltaic applications, including tandems with silicon, ii) the prototypical methylammonium lead iodide perovskite (MAPbI₃) that initially received much attention, but is now less frequently explored owing to the thermal instability of MA,^[6] and iii) the fully inorganic wide-bandgap CsPbBr₃ perovskite aimed toward multi-junction solar cells and light sources, as well as X-ray and gamma-ray detectors.^[45] We show that despite the structural similarity of these materials, they exhibit significantly different behavior in the dynamic processes of charge carriers across different temperature- and excitation-density regimes. We demonstrate that the temperature evolution of charge-carrier dynamics in $FA_{0.83}Cs_{0.17}PbBr_{0.6}I_{2.4}$ is dominated by changes in radiative recombination with only a small contribution arising from trap-mediated processes and that effective charge-carrier mobilities are limited mostly by intrinsic processes, indicating that this material is already highly optimized, allowing only for marginal further efficiency gains. Charge-carrier dynamics in MAPbI₃ are governed by non-radiative mono- and bimolecular processes at room temperature, and energetic disorder and low-bandgap minority-phase inclusions at low temperatures, making low-temperature applications a particular challenge. Finally, CsPbBr₃ is entirely dominated by non-radiative, single charge-carrier trapping at high and low temperatures, and exhibits a notable reduction in conductivity at low temperatures because of significant exciton formation, highlighting the need for improvements in processing methods for wide-bandgap metal-halide perovskite semiconductors.

2. Results and Discussion

2.1. Combinatorial Transient Microwave Conductivity and Photoluminescence Experiment

Figure 1a shows a schematic of our custom-designed and custom-built experimental apparatus allowing for simultaneous acquisition of microwave conductivity and photoluminescence as a function of time after excitation. We built this free-space system by leveraging the recent progress of commercially available optical components in the microwave to terahertz frequency range and the development of fast, high-frequency microwave (MW) detectors. Our unconventional approach adopts high-frequency (102 GHz) microwave radiation (also referred to as millimeter wave), generated from the output of 34 GHz signal generator using a nonlinear frequency multiplier, and launched into free space with a feed horn antenna (see Experimental Section for full details). The radiation is subsequently focused through a thin-film sample, placed in a cryostat for temperature control, and the transmitted microwaves are re-focused onto a detector. The thin film is photoexcited using ultrafast laser pulses (as described in the Experimental Section) and the change in MW transmission intensity deriving from the increase in the sample's

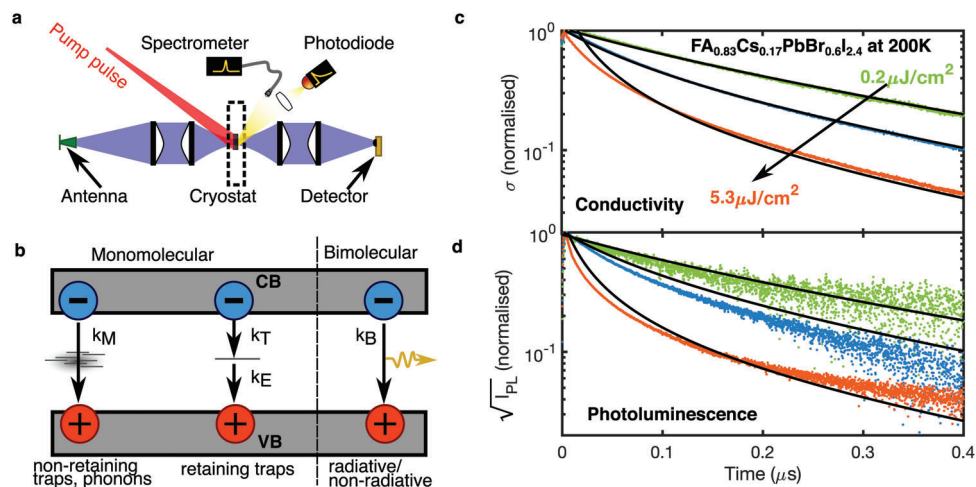


Figure 1. a) A simplified diagram of the combinatorial experimental setup used to acquire photoconductivity decay traces, TRPL data, and PL spectra in situ, showing the feed horn antenna for launching microwave radiation into free space, the fibre-coupled spectrometer and a free-space fast photodiode for PL measurements, and the Schottky diode used to detect transmitted microwave (MW) radiation. b) An illustrated model describing charge-carrier recombination in metal-halide perovskites, encompassing monomolecular and bimolecular recombination routes, and differentiating between charge-retaining and non-retaining traps. The model is used to fit the microwave photoconductivity decay traces shown in (c) globally across different excitation fluences (indicated in the color of the data points) and the obtained parameters of the fits (shown in black solid lines) were used to predict the photoluminescence decay dynamics shown in d). Such predicted PL transients are shown as solid black lines on top of the experimental data (presented as the square root of the PL intensity) with the comparison enabling an assessment of the validity of the assumptions presented in the model.

conductivity is measured as a function of time after the excitation using an oscilloscope. We note that such gigahertz conductivity probes have the advantage of being governed by solely the motion of charge carriers, with ionic conductivity being too slow to follow such high-frequency radiation.^[24] The time resolution of the system is mostly limited by the signal amplifier electronics to ≈ 1 ns. Employing the W-band frequency as a probe of material photoconductivity has many benefits over the low-frequency (6–30 GHz) radiation that has traditionally been used in TRMC experiments.^[46] For example, the shorter wavelength of the probe radiation used here (≈ 3 mm) allows for a tighter focus to be achieved at the sample position, providing better overlap with the optical excitation beam and the potential for higher spatial resolution when probing charge-carrier lifetime variation in non-uniform samples. This approach also enables the investigation of thick (100s of μm) samples of doped semiconductors by offering a higher transmission signal stemming from the reflectance reduction at higher radiation frequencies.^[46] Most importantly, shorter wavelengths allow for collimation of the microwaves using manageably small components enabling free-space propagation of the probing radiation. This free-space approach yields a highly flexible system compared to the traditional method in which transient microwave conductivity changes are probed through the change in the Q-value of a microwave cavity in which the sample is placed. As a result, we are able to conduct in situ experiments simultaneously with the transient photoconductivity measurements, as well as integrate an optical cryostat into the system to enable ease of sample temperature control down to 4 K. In this study, we use a fibre-coupled spectrometer to record the time-integrated emission spectra emitted from the sample, and a fast photodiode detector with a spectral filter to measure TRPL transients integrated across the full emission wavelength range. Such simultaneous photoconductivity and photoluminescence

measurements of the metal-halide perovskites under investigation allow us to carry out concurrent data acquisition under exactly the same experimental conditions, which is crucial to an accurate analysis of the complex charge-carrier recombination processes. In addition, we note that cavity-free TRMC allows for measurements of highly doped semiconducting thin films and can increase the time resolution of the experiment by eliminating the cavity-response time.

2.2. Dynamic Model Capturing Both Conductivity and Photoluminescence Dynamics

In order to model the recorded photoinduced conductivity and luminescence transients, we employ a set of rate equations describing the dynamics of a photoexcited density of charge carriers. The model utilized is similar to those previously deployed by us^[34] and others^[28,35,41,44] to capture the plethora of charge-carrier recombination and trapping processes present in metal-halide perovskites shown schematically in Figure 1b. Due to the low charge-carrier densities employed in the study, we consider only first-order monomolecular and second-order bimolecular processes in our model,^[16] while omitting the third-order recombination process which involves interactions of three charge carriers and therefore only becomes relevant at very high excitation densities.^[47] Bimolecular recombination, described by the rate constant k_{Bi} , is mostly attributed to the radiative recombination of electrons in the conduction band with holes in the valence band arising as an inverse-absorption process.^[48] However, it has been postulated that bimolecular processes could also have a slightly non-radiative component, an example of which is trap-assisted Auger recombination.^[49,50] Monomolecular recombination, on the other hand, stems from the interactions of individual charge

carriers with phonons and defects in the material. Here we identify two distinct cases: i) a single-electron or single-hole trapping mechanism, where an electron (or hole) is quickly captured by a defect with trapping rate k_T but subsequently escapes to recombine with a hole (or electron) on a much slower timescale, with a rate constant k_E , and ii) trap- or phonon-mediated recombination where the capture of the charge carrier and the recombination with its counterpart happens on similar timescales with the rate k_M .^[28,34,51] We note that Mechanism ii is essentially a special case of Mechanism i, for the scenario that the escape rate $k_E n_T p \gg k_T n$ (where n and p are the populations of free electrons and holes, respectively, and n_T is the population of trapped electrons), but we find that the inclusion of both processes is necessary to explain the charge-carrier dynamics in some of the metal-halide perovskites investigated, likely because of different natures of defects at the grain boundaries and in the bulk of the material.^[52] Point defects in these materials are generally highly specific toward the capture of either electrons or holes,^[53,54] as for example halide interstitials acting as electron traps.^[20,55]

We capture the above-mentioned recombination processes in a set of coupled differential equations that describe the time evolution of the electron density populations in the conduction band n and trapped-electron density n_T in a photoexcited intrinsic semiconductor, as follows,

$$\frac{\partial n}{\partial t} = -k_{Bi}np - k_M n - k_T n \quad (1a)$$

$$\frac{\partial n_T}{\partial t} = k_T n - k_E n_T p \quad (1b)$$

where $p = n + n_T$ is the density of free holes in the valence band and the rate constants are as described above.

To determine the time evolution of the photoinduced conductivity σ of the thin film we sum over the conductivity contribution from both electrons and holes, that is

$$\sigma = \mu_e ne + \mu_h pe = \frac{\mu_{cc}}{2}(n + p) \quad (2)$$

where μ_e and μ_h are the individual mobilities of electrons and holes, and μ_{cc} represents their sum. Here, we have assumed $\mu_h = \mu_e$ because these values have previously been shown to be very similar in lead-halide perovskites,^[51,56,57] due to the balanced effective masses of charge carriers,^[2,58–61] leading to a conductivity proportional to the sum of free electron and hole population densities.

The intensity of the photoluminescence I_{PL} emitted as a result of radiative recombination between electrons and holes is proportional to their densities and the bimolecular recombination rate constant k_{Bi}

$$I_{PL} \propto k_{Bi}np \quad (3)$$

leading to a dependence on the product of free electron and hole populations.^[44,51,62]

Importantly, the numerical solution to the Equations (1a) and (1b) then allows the determination of *both* photoinduced conductivity (from Equation (2)) and photoluminescence (from Equation (3)) as a function of time after excitation. The dual comparison with two different experimental observables, measured

under exactly the same conditions in situ, thus allows for an accurate evaluation of the model and extraction of the associated parameters. Figure 1c shows an example for the case of the $\text{FA}_{0.83}\text{Cs}_{0.17}\text{PbBr}_{0.6}\text{I}_{2.4}$ perovskite thin film at a temperature of 200 K. Here, the measured photoinduced conductivity data has been modeled with Equation (2) based on the solutions to Equations (1a) and (1b), optimizing parameters k_T , k_E , k_{Bi} , and k_M for best fits with the data (see Section S1, Supporting Information for the details of the fitting procedure and Sections S2 and S3, Supporting Information for the outputs). The figure also shows the solution to Equation (3), predicting the corresponding decay of the photoluminescence intensity, based on the same fitting parameters, and plotted on top of the TRPL data, showing good agreement. Such modeling of the combinatorial microwave conductivity and photoluminescence transients across a wide range of temperatures and fluences is applied to three key metal-iodide perovskites, as discussed below, and found to be a powerful analytical tool to unravel their dominant mechanisms of charge-carrier recombination. We note that the excitation fluences used in our study of TRMC and TRPL ($0.1\text{--}12 \mu\text{J cm}^{-2}$, depending on the temperature and sample investigated—see Supporting Information for details) correspond to photoexcited charge-carrier density between 10^{16} and 10^{18} cm^{-3} .

2.3. $\text{FA}_{0.83}\text{Cs}_{0.17}\text{PbBr}_{0.6}\text{I}_{2.4}$: A Well-Optimized Direct-Bandgap Semiconductor

We first examine the mixed-halide, mixed-cation perovskite $\text{FA}_{0.83}\text{Cs}_{0.17}\text{PbBr}_{0.6}\text{I}_{2.4}$, highly relevant for photovoltaic applications, including perovskite-silicon tandem solar cells. While the mixed-cation FACS combination allows for the structural stabilization of the material against deterioration into non-perovskite phases,^[63] the absence of the thermally volatile MA further enhances resistance against heat-induced degradation.^[6,64] Meanwhile, the bandgap of 1.67 eV is elevated compared to that of the iodide-only composition (see Table S3, Supporting Information), moving it closer to the ideal value for top layers in tandem cells with silicon,^[10,11] without entering the regime of bromide content above 20% for which these materials are known to be unstable toward halide phase segregation.^[12,13] Single-junction solar cells based on similar compositions have shown power conversion efficiencies of 20.1%,^[15] while tandems with silicon exceeded 30%.^[14,65,66]

Figure 2 highlights the key optoelectronic properties of a solution-processed $\text{FA}_{0.83}\text{Cs}_{0.17}\text{PbBr}_{0.6}\text{I}_{2.4}$ thin film, displaying how the emission, conductivity, and charge-carrier dynamics vary sensitively with temperature. As shown in Figure 2a, the emission intensity measured just after the photoexcitation, which is proportional to the radiative bimolecular recombination constant (see Equation (3)), decreases with increasing lattice temperature of the semiconductor. Such reduction in the radiative bimolecular recombination rate is attributed to the broadening of the electrons' and holes' Fermi–Dirac distributions in their respective bands with rising lattice temperature, which leads to a lower probability of radiative transitions in direct-bandgap semiconductors.^[48,67] Figure 2b clearly supports this underlying mechanism by revealing spectral broadening of the photoluminescence that increases gradually toward high temperatures.

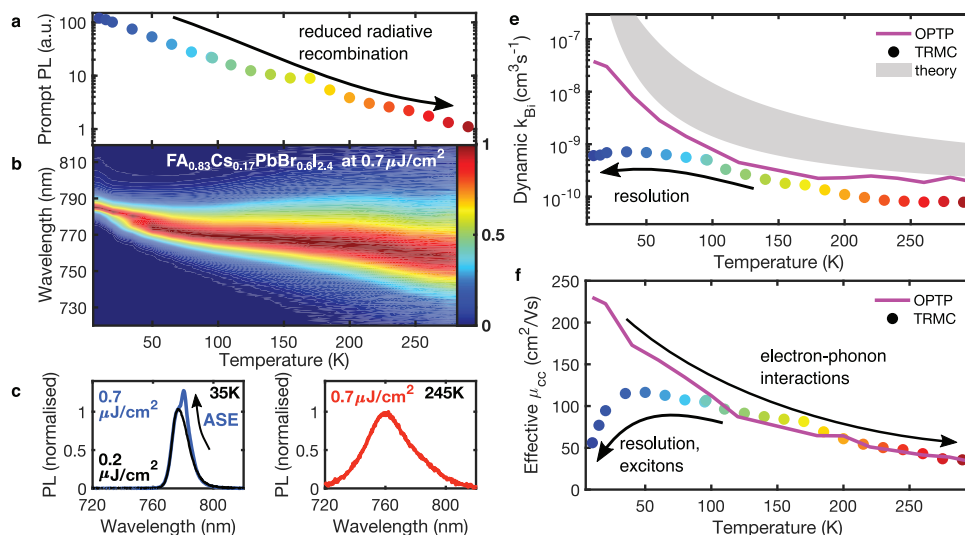


Figure 2. Temperature-dependent optoelectronic properties of a thin film of $\text{FA}_{0.83}\text{Cs}_{0.17}\text{PbBr}_{0.6}\text{I}_{2.4}$ perovskite. a) Prompt PL intensity—the intensity at the time immediately following photoexcitation, for PL transients shown in Figure S2, Supporting Information, shown as a function of temperature. The color of the data points corresponds to the color of the traces shown in the Supporting Information. b) The corresponding time-integrated emission spectra normalized at their peak as a function of temperature. Example spectra for the sample lattice temperature of c) 35 K and d) 245 K, with the spectrum of the perovskite at low temperature also showing the appearance of a narrowed amplified spontaneous emission peak at high excitation fluence. e) Bimolecular recombination rate constant k_{Bi} as a function of temperature, extracted from fits to microwave photoconductivity decays (colored dots, from decays shown in Figure S1, Supporting Information) and to THz photoconductivity transients (magenta line, from decays shown in Figure S7, Supporting Information). The grey shaded area shows the behavior predicted from detailed-balance models, in the presence or absence of Coulombic interactions (top and bottom bound, respectively) according to Ref. [48]. f) The extracted effective electron–hole sum mobility, $\phi\mu_{\text{cc}}$, obtained from microwave (dots) and THz (magenta line) photoconductivity decay traces.

We find that at very low lattice temperatures and/or high excitation density, additional changes to the spectral width originate from amplified spontaneous emission (ASE), as seen in the outlines of the photoluminescence spectrum at 35 and 245 K, shown in Figures 2c and 2d, respectively. ASE contributes to faster radiative recombination of charge carriers and is evident in the emission spectrum as a sharp sub-peak whose intensity varies nonlinearly with excitation fluence.^[68] Such ASE thus leads to a perceived elevated bimolecular band-to-band recombination rate whose cause is difficult to discern solely from conductivity data, highlighting the importance of combinatorial approaches that also monitor photoluminescence concurrently.^[68,69]

We further assess the temperature dependence of the bimolecular band-to-band recombination constant k_{Bi} , by extracting values from global fits of our model to photoconductivity decay traces recorded for a range of excitation fluences (shown in Figure S1, Supporting Information). The solid dots in Figure 2e show the increase in k_{Bi} toward lower temperatures, in broad agreement with the increase in photoluminescence emission rate displayed in Figure 2a. However, a deviation from this monotonic increase can be seen for temperatures around and below 50 K, for which the extracted bimolecular recombination rate appears to plateau. To uncover the origin of this discrepancy, we also perform an OPTP measurement (details of which can be found in the Experimental Section and Section S5.1, Supporting Information), accessing the photoconductivity decay dynamics on much shorter timescales (of up to ≈ 1 ns) and higher time resolution (sub-picosecond) than attainable with the TRMC setup (resolution ≈ 1 ns, observation range 200 μs).

We find that the bimolecular recombination constant k_{Bi} extracted from OPTP conductivity transients, as shown by the magenta line in Figure 2e, exhibits a continued pronounced rise toward low temperatures, closely matching the trend obtained from the theory of detailed balance between radiative transitions in direct-bandgap semiconductors originally observed by Davies et al. for lead iodide perovskite semiconductors (grey shaded area in the same figure).^[48] We therefore attribute the deviation of k_{Bi} extracted from TRMC measurements to the limited nanosecond time resolution of such measurements that are inherent to the electronic time-gating approach of TRMC, as opposed to the optical gating employed in OPTP. Our comparison thus reveals that even our new millimeter-wave-based TRMC system, which displays enhanced time resolution owing to the absence of a cavity-response time, cannot adequately capture the significant amount of bimolecular recombination occurring in the first nanosecond after photoexcitation at low sample temperatures.

We further examine the effective sum charge-carrier mobility $\phi\mu_{\text{cc}}$ of the material, where ϕ is the photon-to-free-charge-carrier branching ratio.^[70] In the absence of exciton formation, $\phi=1$ may be assumed because all absorbed photons create free charge carriers that contribute to a conductivity response, which has been shown to hold for most 3D metal-halide perovskites at room temperature^[70,71] (see Section S6, Supporting Information for further details). Figure 2f shows $\phi\mu_{\text{cc}}$ as extracted from TRMC (filled dots) and OPTP (magenta line) photoconductivity values immediately after excitation (see Sections S4.1 and S5.1, Supporting Information for details). The decrease

of mobility with rising temperature in metal-halide perovskites has been previously investigated and attributed to increased Fröhlich coupling between charge carriers and longitudinal optical phonons.^[18,29,71–74] However, we note that effective mobility values extracted from microwave conductivity measurements remain below those extracted from OPTP at low temperatures. This effect stems from two independent processes, both present in our experiment. First, the rapid charge-carrier recombination occurring at low temperatures within the limited time resolution of the system, as described above, reduces the conductivity apparent in the early part of the transient, leading to an underestimation of the extracted mobility values. Second, exciton formation, more prevalent at low temperatures, decreases the photon-to-free-charge-carrier branching ratio ϕ (as discussed in Section S6, Supporting Information) and therefore the effective sum charge-carrier mobility $\phi\mu_{cc}$. The sensitivity of millimeter and THz waves to excitons significantly depends on the frequency of the probe. The localized nature of excitonic states leads to resonances that display a clear non-Drude conductivity that has a rising from zero trend with increasing frequencies.^[71,75,76] Therefore the relatively low-frequency (0.1 THz) microwave measurements will mostly be insensitive to excitons, while OPTP experiments, performed in the 0.5–2.5 THz frequency range^[71,75–77] may display a partial sensitivity to excitons with relatively low binding energy, as for example, the value of around 10 meV determined here for MAPbI₃ (see Section S6, Supporting Information).

Importantly, we find that for FA_{0.83}Cs_{0.17}PbBr_{0.6}I_{2.4} film, fits to the microwave conductivity transients with our model described above also reproduce the PL transients highly accurately (see Figure 1c for an example, and Figure S2, Supporting Information for all transients). This observation highlights that, unlike the low-temperature dynamics for CsPbBr₃ discussed further below, the kinetics of charge-carrier recombination in FA_{0.83}Cs_{0.17}PbBr_{0.6}I_{2.4} are well described by the simple rate equation model based on trapping, trap emptying, and radiative band-to-band recombination. Fits based on this model further determined a relatively low trap-mediated recombination rate of $k_T = 8.5 \times 10^6 \text{ s}^{-1}$ at room temperature, which decreases further at lower temperatures, indicating the suppression of non-radiative recombination processes^[18,71] (see Table S1, Supporting Information for extracted fitting parameters). Because of this suppression of monomolecular recombination and the concomitant increase of radiative recombination strength, dynamic processes become dominated by intrinsic radiative electron–hole recombination at lattice temperatures below 110 K and charge-carrier densities of 10^{16} cm^{-3} (comparable to those present under solar illumination^[78]). Moreover, the temperature trend of the bimolecular recombination constant is accounted for by changes in the Fermi–Dirac distribution of photoexcited charge carriers, as concluded from the evolution of the photoluminescence emission spectra and the photoinduced conductivity dynamics. Finally, the high charge-carrier mobility observed in FA_{0.83}Cs_{0.17}PbBr_{0.6}I_{2.4} indicates that current solution processing methods are well optimized for the deposition of high-quality films, in which the electronic mobility is mostly limited by electron–phonon interactions, an intrinsic process that cannot be circumvented via improvements in material synthesis.

2.4. MAPbI₃: Low-Temperature Energetic Disorder Impacted by Phase Transitions

We proceed by examining the charge-carrier dynamics in a prototypical MAPbI₃ solution-processed film (bandgap of 1.64 eV—see Table S1, Supporting Information), disentangling intrinsic (fundamental) from extrinsic (material quality) processes. Numerous studies have investigated this composition as a representative example of the perovskite family,^[18,22,70,79] owing to its success in the early-stage development of lead-halide perovskite solar cells.^[80,81] From a technological point of view, however, the volatile nature of MA in the structure has since been linked to the thermal and chemical instability of the material,^[6] and most recent high-performance reports of stable solar cells have therefore been based around alternate A-cations, or MA alloyed with other cations across A-sites.^[15,82] On the fundamental photophysical side, MAPbI₃ has still continued to be presumed a material representative of the broad class of lead-halide perovskites. As we show below, the situation is somewhat more nuanced, with MAPbI₃ retaining idiosyncratic features of some energetic disorder and trap-mediated recombination that are largely absent in the high-performance FA_{0.83}Cs_{0.17}PbBr_{0.6}I_{2.4} film discussed above.

As the summary of experimental observations for MAPbI₃ presented in Figure 3 shows, the general temperature trends of prompt photoluminescence and bimolecular recombination rate constants are similar to those for FA_{0.83}Cs_{0.17}PbBr_{0.6}I_{2.4}. As the temperature is reduced, bimolecular band-to-band recombination, in general, appears to increase with decreasing temperature, again indicating a sharpening of the electron- and hole-thermal distributions across the conduction and valence bands. However, there are three notable deviations from this general trend, which we discuss in turn.

First, we find that the low-temperature structural phase transition in the MAPbI₃ thin film clearly affects the dynamics of photoexcited charge carriers. We note that although single-crystal MAPbI₃ undergoes the orthorhombic-to-tetragonal phase transition at 160 K,^[83,84] the transition temperature can vary for thin films owing to strain and inhomogeneity in polycrystalline materials.^[27,85,86] In our MAPbI₃ thin film, the low-temperature phase transition occurs near $\approx 150 \text{ K}$. Just below this transition, a deviation from the underlying trend in k_{Bi} (Figure 3c) and a significant discontinuity of the emission strength (Figure 3a) are apparent. We attribute this phenomenon to the existence of small tetragonal phase inclusions between 100 and 150 K in the material^[27] which have previously been shown to co-exist with the low-temperature orthorhombic majority phase, possibly as a result of strain in the film that leads to regional variations in the phase transition temperature.^[86] We suggest that the lower bandgap of MAPbI₃ in its tetragonal phase leads to a funneling of charge carriers into these inclusions and an increase of the local charge-carrier density, which in turn strengthens the radiative recombination. As a result, both the bimolecular recombination rate constant (Figure 3c) and the prompt photoluminescence (Figure 3a) suddenly increase as the temperature is lowered below 150 K, and they revert to the underlying trend around $\approx 100 \text{ K}$, for which remnant structural phases have been largely eliminated.

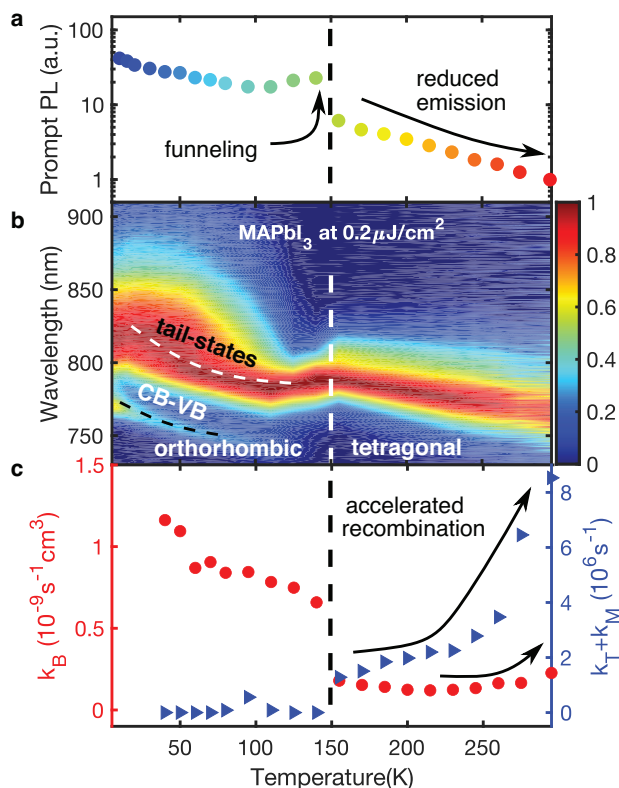


Figure 3. Temperature evolution of emission and conductivity of a MAPbI₃ thin film: a) prompt PL intensity, b) emission spectrum, and c) dynamic decay rates, with the phase transition indicated by a dotted line around 150 K. The prompt PL intensity was extracted from PL transients shown in Figure S4, Supporting Information. The bimolecular and monomolecular decay constants were extracted from fits of the model described by Equations (1a) and (1b) to microwave conductivity transients shown in Figure S3, Supporting Information. The value of $k_M + k_T$ represents the total monomolecular recombination rate of charge carriers.

Second, we find that at very low temperatures and low excitation density, most of the emission from MAPbI₃ does not originate from the direct conduction-band-to-valence-band transitions, but rather from the recombination of the charge carriers in band tail states, that is, traps with a broad energetic density distribution formed immediately below the band-edge states.^[21,25] Such band tail emission is apparent from the time-integrated photoluminescence spectra shown in Figure 3b, which display a very broad emission peak at wavelengths longer than the sharp band-edge emission, for temperatures below ≈ 120 K. At high excitation densities, these tail states become saturated and the high-energy, band-to-band recombination dominates the emission spectrum, as seen in Figure S12, Supporting Information. We note that while the presence of the band tails does not significantly affect the charge-carrier recombination dynamics in MAPbI₃ observed from photoconductivity transients, the low-temperature effective charge-carrier mobility is clearly impacted, showing a decline toward lower temperatures, as displayed in Figure S11, Supporting Information.

Third, we find a region near room temperature where band-to-band recombination has a mildly temperature-activated component. Figure 3c shows that between 200 and 300 K, the bi-

molecular band-to-band recombination rate constant (k_{Bi} , red solid circles) increases slightly with increasing lattice temperature. This increase coincides with a significant rise in the total monomolecular trap-mediated recombination constant ($k_M + k_T$, blue solid triangles). This strong correlation in trends between k_{Bi} and monomolecular recombination rates suggests that a process related to charge trapping is responsible for the rise of bimolecular recombination above 200 K. Trap-mediated processes tend to increase with increasing temperature, both because Shockley–Read–Hall recombination is temperature dependent and because traps themselves exist within a thermal equilibrium with the “perfect” lattice, leading to a shift toward a more defective lattice at higher temperatures.^[87] We therefore propose that trap-mediated Auger recombination, in itself a bimolecular process,^[50] causes the slightly temperature-activated behavior for k_{Bi} between 200 and 300 K, rather than an intrinsic effect associated with indirect gaps arising from Rashba effects, as had previously been suggested.^[18] Such a trap-mediated Auger recombination will operate in parallel to intrinsic free electron–hole recombination, imparting a slightly non-radiative component to the overall bimolecular recombination.^[49] The strong correlation we observe with the presence of non-radiative recombination in MAPbI₃, and the absence of such processes for FA_{0.83}Cs_{0.17}PbBr_{0.6}I_{2.4} (see Section 2.3) shows that such second-order non-radiative processes are related to material quality, rather than being intrinsic to lead halide perovskite semiconductors. Additionally, trap-mediated Auger recombination rates may be highly trap specific: calculations have suggested that energetically deep traps mediate Auger recombination more effectively than shallow traps in metal-halide perovskites.^[88] Here we indeed observe such a correlation of non-radiative bimolecular recombination with the nature of traps. Our fits to microwave conductivity transients based on the rate equation model show that for MAPbI₃, strong monomolecular recombination occurs through defects that do not retain charge carriers, while the charge-carrier recombination in FA_{0.83}Cs_{0.17}PbBr_{0.6}I_{2.4} appears to be impacted only by electron-retaining traps (see Tables S1 and S2, Supporting Information). This difference may be caused by a prevalence of shallow traps in mixed-cation, mixed-halide perovskites, and deep traps in MAPbI₃, explaining why only MAPbI₃ exhibits such non-radiative bimolecular recombination arising from trap-mediated Auger processes, while this effect is absent in FA_{0.83}Cs_{0.17}PbBr_{0.6}I_{2.4}.

Our findings reveal that, compared to best-in-class lead-halide perovskites, MAPbI₃ films are relatively susceptible to disorder at low temperatures. Optoelectronic properties of MAPbI₃ films are strongly affected by phase transitions, in sharp contrast to what is observed for the FA_{0.83}Cs_{0.17}PbBr_{0.6}I_{2.4} perovskite. In addition, a higher propensity toward deep trap formation than observed in FA_{0.83}Cs_{0.17}PbBr_{0.6}I_{2.4} leads to trap-mediated Auger recombination, imparting a slightly non-radiative component to bimolecular recombination near room temperature in MAPbI₃ thin films.

2.5. CsPbBr₃: Partly Excitonic System Dominated by Electron Trapping

As a third lead-halide perovskite, we investigate a fully inorganic, thermally evaporated CsPbBr₃ thin film. Lead-bromide

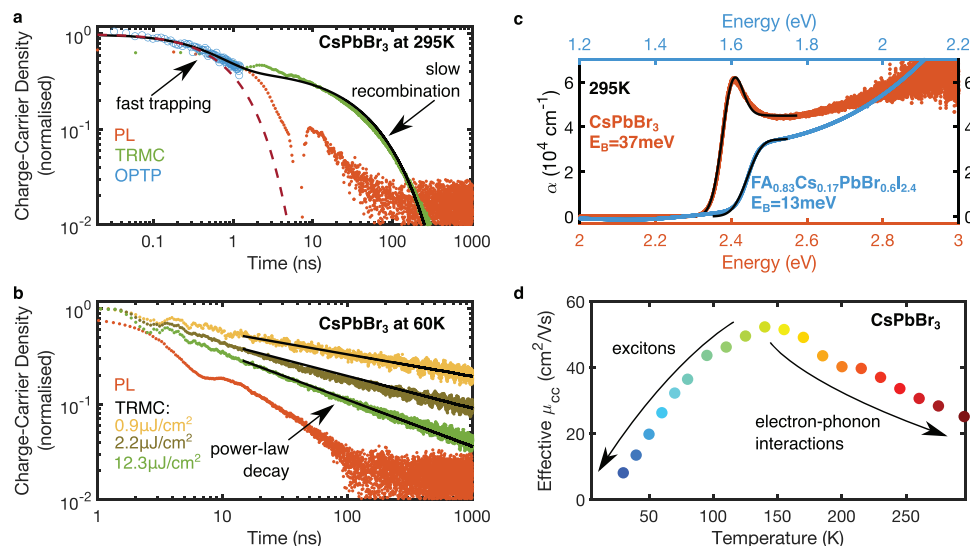


Figure 4. Optoelectronic properties of a thermally evaporated CsPbBr₃ perovskite thin film. a) Room-temperature charge-carrier decay dynamics, represented by the decay of THz photoconductivity (open blue circles), MW conductivity transients (green dots), and photoluminescence signal decay (square root of intensity, shown as orange dots). The black solid line represents the fit to the conductivity data resulting from the model described in the main text. The dashed red line shows the predicted transient of the PL intensity. b) Microwave photoconductivity decays at 60 K, shown in yellow, brown, and green dots for different excitation fluences indicated by legend colors matching those of the datapoints. The square root of PL intensity is shown in orange dots. Black solid lines show power-law fits to the microwave data. c) Absorption onsets of CsPbBr₃ and FA_{0.83}Cs_{0.17}PbBr_{0.6}I_{2.4} at room temperature, shown as orange and blue dots, respectively. Black lines show fits according to the Elliott function^[89] and the extracted exciton binding energies are indicated in the color matching that of the datapoints. d) Dependence of effective electron–hole sum mobility on temperature, extracted from microwave photoconductivity traces (as outlined in Section S4.1, Supporting Information) shown as solid dots, whose colors match those of the conductivity transients presented in Figure S5, Supporting Information.

perovskites offer significantly larger bandgaps than their iodide counterparts, with CsPbBr₃ thin film exhibiting a bandgap energy of 2.44 eV, as listed in Table S3, Supporting Information. Such wide-bandgap perovskites are particularly important for realizing highly efficient light-emitting diodes and lasers, X-ray and gamma-ray detectors,^[45] as well as multi-junction solar cells, in which they may be employed as top active layer.^[90] It has been shown that the poor solubility of caesium halide salts, particularly CsBr₂, in solvents commonly used for perovskite deposition limits the quality of solution-processed wide-bandgap films.^[91,92] The thermal evaporation method employed here provides a more promising alternative, with added benefits of avoiding solvent-orthogonality problems in multi-layer devices, and more accessible routes toward industrial upscaling.^[93] Single- and multi-junction solar cells incorporating high-bandgap perovskites as active layers have reached power conversion efficiencies of 10.9% and 20.1%, respectively.^[90,94]

We first focus our analysis on the charge-carrier dynamics in CsPbBr₃ at elevated temperatures, for which Figure 4 shows an example at 295 K (see Figure S5, Supporting Information for all transients recorded between 30 and 295 K). We find that at ambient temperature, the electronic processes in the CsPbBr₃ film are heavily dominated by selective trapping of one of the two charge-carrier species. In contrast to the dynamics discussed for iodide-rich perovskites above (see Figure 1c,d), for CsPbBr₃ the TRPL intensity (a square root of which is shown in orange dots in Figure 4a) decays on much faster timescales than the microwave photoconductivity (presented as green dots in the same figure). Furthermore, the conductivity transients presented in Figure S5, Supporting Information show a distinct lack of excitation-fluence

dependence, indicating strong monomolecular recombination pathways. Taken together, these observations suggest that one charge-carrier species is effectively trapped, extinguishing the luminescence that relies on the presence of both types of charge carriers, while leaving a long-lived element of conductivity arising from just the remaining species. We attribute this effect to the presence of a high density of bromide interstitial defects in the investigated film, which has been shown to trap photoexcited electrons on ultrafast timescales, with the subsequent recombination of the trapped electrons with free holes lasting up to microseconds.^[20]

Next, we show that these observations can be accurately explained by our charge-carrier recombination model captured in Equations (1a) and (1b) in the presence of a strong single charge-carrier trapping mechanism with a slow emptying rate (large $k_{-T}n > k_E p n_T$). As Equations (2) and (3) indicate, the fast depletion of free electrons from the conduction band will lead to significant quenching of photoluminescence, with significant remnant conductivity arising from free holes. We confirmed the existence of such fast electron trapping, which may be partly missed by the nanosecond time resolution of the TRMC experiment, through an additional OPTP measurement with sub-picosecond time resolution (open blue circles in Figure 4a, for excitation-fluence dependence see Figure S8, Supporting Information) which reveals a rapid and significant reduction of photoinduced conductivity in CsPbBr₃. We have successfully modeled the full evolution of the charge-carrier population within this scenario using rate equations very similar to Equations (1a) and (1b) (Equation (S4), Supporting Information, see the black solid line fit to the data in Figure 4a). We note that for the case of CsPbBr₃, the slow

recombination of trapped electrons with free holes was best described by the Kohlrausch–Williams–Watts (KWW) function (which in the absence of other recombination pathways results in stretched exponential decay $\propto e^{-(k_{\text{KWW}}t)^\beta}$),^[95,96] as previously determined for this kind of trap–escape process.^[97] We find that the model reproduces the observed dynamics of photoinduced conductivity highly accurately, as well as reproducing the photoluminescence transient (plotted as a dashed orange line in the same figure), confirming the strong dominance of trapping and the suitability of the model to predict the evolution of the charge-carrier population (details of the modeling and the outputs of the fitting procedure are shown in Section S5.2, Supporting Information).

We further demonstrate that the charge-carrier dynamics in CsPbBr₃ drastically change upon cooling toward low temperatures and can no longer be adequately captured by the model described by Equations (1a) and (1b), and Equation (S4), Supporting Information. Figure 4b reveals that the photoconductivity at 60 K exhibits a power-law decay ($\propto t^{-\alpha}$), significantly deviating from the charge-carrier population evolution at room temperature. Such power-law decays are usually associated with an abundance of localized, energetically shallow traps in a semiconductor.^[25,98–100] These traps may form an exponential density distribution of near-band-edge energy levels, causing charge-carrier localization and subsequent slow thermal de-trapping allowing delayed band-to-band recombination.^[25,97] Interestingly, previous investigations showed this effect to occur only in perovskite compositions containing large polar organic cations, such as MA or FA,^[25,97] for which they have been attributed to polar disorder. Here, we report the presence of power-law recombination also for perovskites incorporating fully inorganic, non-polar, caesium A-cations. We propose that for CsPbBr₃ such band tail states may therefore originate from a disorder of a different kind, for example, associated with the high density of trapped charges, and may therefore potentially be eliminated through further improvements in synthesis schemes.

Finally, we show that for CsPbBr₃, intrinsic exciton formation has a clear impact on the fundamental optoelectronic properties, in particular at low temperatures. Such difference with their iodide-rich counterparts should be expected, given the higher exciton binding energies for bromide perovskites compared with iodide perovskites.^[101,102] Figure 4c illustrates this effect through the room-temperature absorption spectrum near the absorption onset for the CsPbBr₃ film (orange dots), contrasted with that of the FA_{0.83}Cs_{0.17}PbBr_{0.6}I_{2.4} film (blue dots). The former shows a much stronger exciton absorption peak near the band edge than the latter, suggestive of a higher exciton binding energy. To quantify such effects and disentangle them from the potential difference in spectral broadening (which could also result in apparent changes of excitonic resonance intensity^[101]), we fitted an Elliott function^[89] (see Section S6.1, Supporting Information for details) capturing the absorption spectrum in the presence of Coulomb interactions (shown in black solid lines on top of the data) and extract a significantly higher exciton binding energy of 37 meV for CsPbBr₃ compared to the value for FA_{0.83}Cs_{0.17}PbBr_{0.6}I_{2.4} (13 meV). Importantly, such enhanced Coulomb interactions in the wide-bandgap lead-bromide perovskites are also found to cause lower photon-to-free-charge-carrier conversion ratios ϕ at low temperatures, as Figure S10, Supporting Information clearly

demonstrates. As Figure 4d shows, these effects manifest as a significant reduction in the effective mobility $\phi\mu_{\text{cc}}$ extracted from TRMC below 150 K that cannot solely be explained by limits in the time resolution of the setup. Because microwave radiation does not couple effectively to excitons with such binding energies, our probe is effectively “blind” to their presence, and instead only detects the response of free charges. Given that excitons as charge-neutral species do not respond to the presence of electric fields of low strength, such a strong lowering of effective mobility will adversely affect real transport properties at low temperatures.

Our observations show that the optoelectronic properties of the thermally evaporated CsPbBr₃ perovskite films are heavily influenced by the formation of electron-trapping defects around room temperature, and by excitonic effects as well as the energetically shallow tail of sub-band trap states at low temperatures. Since exciton formation is an intrinsic effect occurring in this perovskite material, low-temperature applications of lead-bromide perovskites (such as cryogenically cooled photodetectors) will remain limited, given the poor photon-to-electron conversion efficiency. At room temperature, however, exciton formation is less important even for lead-bromide perovskites, and material optimization instead needs to focus on the elimination of traps, such as bromide interstitials, through improvements in processing methods for these important wide-bandgap perovskite semiconductors.

3. Conclusion

We have demonstrated a powerful combinatorial approach to uncover the charge-carrier kinetics for three key lead-halide perovskites, each displaying distinct recombination and trapping regimes. Our custom-built experiment allowed for the simultaneous in situ acquisition of TRMC without use of a cavity and time-resolved and spectrally resolved photoluminescence emission across a wide temperature range. Analyzing such temperature- and excitation-fluence-dependent data through an analytical model capturing trapping, de-trapping, and recombination events for both conductivity and luminescence allowed for unambiguous disentanglement of such processes in FA_{0.83}Cs_{0.17}PbBr_{0.6}I_{2.4}, MAPbI₃, and CsPbBr₃ thin films. We also found that overall, values and trends reported in the literature^[15,18,20–22,25,27,48,64,71,79,86,93,97–100] for each of the three compositions, when examined with just one of the individual techniques, agree well with our findings, suggesting that the compositions and preparation methods used in our study represent well those commonly employed in the field.

For solution-processed FA_{0.83}Cs_{0.17}PbBr_{0.6}I_{2.4} films, now well optimized for high photovoltaic device performance, we found the temperature dependence of the optoelectronic properties to be well described by the radiative band-to-band recombination typical of a direct-bandgap semiconductor. Thus, while FA_{0.83}Cs_{0.17}PbBr_{0.6}I_{2.4} still exhibits some element of trap-mediated recombination at charge-carrier densities of 10¹⁶ cm⁻³, such pathways are less frequently taken than intrinsic radiative pathways at temperatures below 110 K. The evolution of emission spectra, prompt PL intensity and dynamic bimolecular recombination constant all indicated typical intrinsic behavior, with radiative recombination increasing toward low temperature as the thermal distribution of charge carriers across the bands

is narrowed, and charge-carrier mobilities rising as coupling to longitudinal phonon modes is suppressed. In addition, no significant changes in these properties were observed to arise from structural phase transitions. These results are a testament to the high quality of these mixed FACs A-cation perovskites that are now approaching intrinsic performance limits in solar cells.^[15]

The solution-processed MAPbI₃ film, commonly used as a representative of the whole family of metal-halide perovskites, shares general trends with FA_{0.83}Cs_{0.17}PbBr_{0.6}I_{2.4}, but also exhibits several important differences. MAPbI₃ displays substantial energetic disorder in the low-temperature orthorhombic phase, manifesting through sub-bandgap emission from tail states at low temperatures and through charge-carrier funneling effects arising from spatial structural inhomogeneities across the film at temperatures just below the phase transition, where both the orthorhombic and the tetragonal phases co-exist. At room temperature, the presence of traps is found to correlate with both first-order, monomolecular trap-mediated recombination and second-order trap-mediated Auger recombination, both of which represent non-radiative recombination losses. These findings indicate that MAPbI₃ may require careful trap elimination for optimized room-temperature operation, and may be less suitable for low-temperature applications.

Finally, the wide-bandgap, thermally evaporated, CsPbBr₃ film is shown to be entirely dominated by non-radiative charge-carrier trapping at both high and low temperatures. At temperatures near ambient, charge-carrier dynamics are governed by a large density of traps specific to the capture of just one of the two charge-carrier types, most likely electron-trapping bromide interstitials. Such rapid selective capture of one charge type is evident in both the rapid decay of photoluminescence which requires the presence of both electrons and holes, and the observed two-phase decay of conductivity transients displaying first a rapid capture of electrons followed by the slow decay of free holes. At low temperatures, a power-law decay of conductivity transients is observed, consistent with an exponential density distribution of shallow energetic traps close to the band edges. Finally, we found that the elevated exciton binding energy in CsPbBr₃ is responsible for a large fraction of absorbed photons being converted to excitons rather than free charge carriers at moderately low temperatures below 150 K, resulting in a significant reduction of photoconductivity. Overall, these findings highlight the need for further improvements in processing methods, particularly tailored toward reducing the defect densities in wide-bandgap, lead bromide-rich perovskites.

Overall, our study demonstrates that the complex dynamic electronic processes in metal-halide perovskite semiconductors can only be reliably differentiated by considering their effects on multiple observable properties, and their evolution with a range of variables such as temperature and charge-carrier density. Our combinatorial experimental approach thus presents a powerful tool for the assessment of optoelectronic performance parameters in situ, in a manner that is easily transferable to high-throughput screening of materials for solar cell applications.

4. Experimental Section

Sample Preparation: FA_{0.83}Cs_{0.17}PbBr_{0.6}I_{2.4} films were fabricated as follows. 207 mg FAI (Greatcell Solar), 64 mg CsI (Alfa Aesar) 103.8 mg

PbBr₂ (Alfa Aesar), and 538.2 mg PbI₂ (TCI Chemicals) were dissolved in a 3:1 v/v ratio of DMF:DMSO (Sigma-Aldrich) to give a 1.2 M perovskite ink. The ink was then spin coated onto z-cut quartz disks in a drybox (15% RH) using a two-step deposition program: 1000 rpm for 10 s, followed by 6000 rpm for 35 s. For the solvent-quenching step, 300 μL of methyl acetate (Sigma-Aldrich) was quickly deposited onto the spinning substrate 10 s before the end of the program. The substrates were then directly transferred onto a hotplate and annealed for 20 min at 150 °C, after which they were allowed to cool to room temperature naturally. When the substrates were cool a 10 wt% solution of polymethyl methacrylate (PMMA, Sigma-Aldrich, M_w ≈ 15000) in chlorobenzene (Sigma-Aldrich) was spin coated onto the perovskite-coated substrate at 6000 rpm for 45 s. The samples were then kept in a nitrogen-filled glovebox until they were measured. The thicknesses of the bare films were measured using a Dektak surface profilometer to be 320 nm.

MAPbI₃ thin films were prepared using the acetonitrile route as reported previously by Noel et al.^[103] In brief, CH₃NH₃I (MAI, Greatcell Solar Materials), and PbI₂ (TCI Chemicals) were weighed out and dissolved in acetonitrile with methylamine gas to give a 0.5 M CH₃NH₃PbI₃ solution. The solution was then dynamically spin coated onto the z-cut quartz disks in a drybox (26% RH) at 2500 rpm for 45 s. The films were then annealed for 1 h at 100 °C. PMMA solution (as above) was then dynamically spin coated at 6000 rpm for 30 s on top of the perovskite film. The thicknesses of the bare films were measured using a Dektak surface profilometer to be 320 nm.

Thin films of CsPbBr₃ were fabricated using thermal evaporation as reported previously by Patel et al.^[104] In brief, CsBr (ultradry 99.999% [metals basis], Alfa Aesar) and PbBr₂ (ultradry 99.999% [metals basis], Alfa Aesar) were placed in separate crucibles, and the z-cut quartz substrates were mounted on a rotating substrate holder to ensure that a uniform film was deposited. The chamber was allowed to reach a high vacuum (10⁻⁶ mbar), before the CsBr and the PbBr₂ were heated to reach the set deposition rate. Once the deposition rate had stabilized, the substrates were exposed to the vapor. The rates of both CsBr and PbBr₂ deposition were monitored using a quartz crystal microbalance. The final deposition rate was 1 Ås⁻¹. The thicknesses of the films were measured using a Dektak surface profilometer to be 650 nm.

High-Frequency TRMC and PL Spectroscopy: Microwave radiation at 34 GHz was generated using a signal generator, converted to 102 GHz using a frequency tripler, and launched into free space with a standard gain feed horn antenna. The high-frequency, millimeter-wave microwave radiation was focused onto a sample placed in a cold-finger cryostat and re-focused onto a detector with PTFE lenses. The microwave intensity transmitted through the sample was measured with a custom-made GaAs Schottky-diode detector and photoinduced changes in the signal were amplified with a broad-band amplifier made in-house and measured with a fast oscilloscope. The microwave conductivity system was operated in transmission geometry (see the diagram in Figure 1a) with most of the incident microwave signal being transmitted through the sample, and the change in transmission directly upon photoexcitation typically amounting to <5% of the transmitted signal in the absence of photoexcitation, depending on the excitation fluence used. The spectrally resolved photoluminescence was measured using a fibre-coupled spectrometer (Ocean Optics, USB2000+) and TRPL was measured using a spectral filter (to remove laser scatter) and fast photodiode detector, from which the signal was amplified with a broad-band amplifier made in-house and measured with the same oscilloscope as above. The samples were photoexcited with a pulsed laser light originating from Ti:Sapphire amplified laser system (Spectra-Physics, Maitai-Ascend-Spitfire, 35 fs pulse duration), frequency doubled in a BBO crystal to 400 nm central wavelength for investigating CsPbBr₃ and converted to 670 nm central wavelength using an optical parametric amplifier (Light Conversion, TOPAS-C) for investigating MAPbI₃ and FA_{0.83}Cs_{0.17}PbBr_{0.6}I_{2.4}. The choice of the excitation wavelength for each of the materials ensured a long absorption depth of the pump pulse (see Table S3, Supporting Information for bandgap energy values), comparable to the film's thickness, which resulted in a uniform excitation of charge-carrier pairs along the depth of the sample. Such uniform excitation minimized unwanted effects originating from charge-carrier diffusion process,

such as reduction of the photoluminescence intensity caused by decreased carrier density, and simplified the modeling of charge-carrier dynamics. The time resolution of the TRMC system was measured as the rise time (10% to 90%) of the signal to be 1.1 ns for conductivity measurement and 2.6 ns for TRPL traces.

OPTP Spectroscopy: The OPTP experiments were conducted using the method described previously.^[51,77,105,106] The room-temperature measurements were performed using the above-mentioned Ti:Sapphire laser system as an excitation source, employing the OPA and a BBO crystal to generate the same excitation wavelengths as used in the TRMC experiments. THz pulses were generated with a spintronic emitter (2nm-W–1.8nm-Co₄₀Fe₄₀B₂₀–2nm-Pt^[107]) and detected via electro-optic sampling in 1-mm-thick (110) ZnTe crystal. For the temperature-dependent measurements, samples were photoexcited using a Ti:Sapphire amplified laser system (Spectra-Physics, Maitai-Empower-Spitfire) whose central wavelength was converted to 670 nm using an optical parametric amplifier (Light Conversion, TOPAS-C). THz pulses were generated and detected as above. The temperature of the sample was varied using a cold-finger cryostat. The temporal system resolution, defined as the standard deviation of the Gaussian broadening of photoconductivity onset, has been previously measured to be 320 fs.^[108]

Absorption Spectrum: The absorption spectra of the thin films were measured using a Fourier-transform IR spectrometer (Bruker Vertex 80v) with a reflection–transmission attachment, a tungsten-filament lamp as a light source, and a CaF₂ beamsplitter. A silver mirror was used as a 100% reflection/0% transmission reference and an empty sample holder as the 100% transmission/0% reflection reference.

Data Processing: The photoinduced conductivity σ (proportional to the charge-carrier sum mobility μ_{cc} and charge-carrier pair density n) was proportional to the relative change of THz transmission through the thin film^[109]

$$\sigma = n\mu_{cc}e = \frac{\epsilon_0 c(1 + n_{sub})}{d} \frac{\Delta T}{T} \quad (4)$$

where e is the electron charge, ϵ_0 is the vacuum permittivity, c is the speed of light, d is the thickness of the thin-film sample that is photoexcited, $n_{sub} = 2.1$ is the refractive index of the crystalline quartz substrate,^[110] T is the transmitted THz field strength prior to photoexcitation, and ΔT is the difference in the transmission strength with and without photoexcitation. Similarly, the photoconductivity was proportional to the change of microwave transmission in the TRMC experiment, directly measured in the system described above.^[111] Using Equation (4), the sum mobility was extracted from photoconductivity onsets measured at room temperature and shown in Figure S8, Supporting Information, using the known charge-carrier excitation density $n(t=0)$ (Equation (S1), Supporting Information). The values of mobility shown in Figures 2f and 4d were normalized to the effective sum mobility measured at room temperature in order to obtain the temperature-dependent mobility trends.

Supporting Information

Supporting Information is available from the Wiley Online Library or from the author.

Acknowledgements

The authors thank the Engineering and Physical Sciences Research Council (EPSRC) for financial support. A.M.U. thanks the EPSRC Centre for Doctoral Training in Plastic Electronics for financial support. K.A.E. and A.M.U. acknowledge the support of the Rank Prize through a Return to Research grant. N.K.N. thanks EPSRC for support through an Early Career Fellowship (EP/V011197/1). P.G.H. thanks the STFC Centre for Instrumentation. M.B.J. thanks EPSRC for an Established Career Fellowship (EP/T025077/1). L.M.H. acknowledges support through a Hans Fischer Senior Fellowship from the Technical University of Munich's Institute for Advanced Study, funded by the German Excellence Initiative.

Conflict of Interest

The authors declare no conflict of interest.

Data Availability Statement

The data that support the findings of this study are available from the corresponding author upon reasonable request.

Keywords

charge-carrier dynamics, metal-halide perovskites, millimeter wave, optical-pump–terahertz-probe spectroscopy, time-resolved microwave conductivity, time-resolved photoluminescence

Received: May 12, 2023

Revised: July 9, 2023

Published online: August 23, 2023

- [1] H. J. Snaith, *Nat. Mater.* **2018**, *17*, 372.
- [2] L. Protesescu, S. Yakunin, M. I. Bodnarchuk, F. Krieg, R. Caputo, C. H. Hendon, R. X. Yang, A. Walsh, M. V. Kovalenko, *Nano Lett.* **2015**, *15*, 3692.
- [3] J. H. Noh, S. H. Im, J. H. Heo, T. N. Mandal, S. I. Seok, *Nano Lett.* **2013**, *13*, 1764.
- [4] S. A. Kulkarni, T. Baikie, P. P. Boix, N. Yantara, N. Mathews, S. Mhaisalkar, *J. Mater. Chem. A* **2014**, *2*, 9221.
- [5] K. J. Savill, A. M. Ulatowski, L. M. Herz, *ACS Energy Lett.* **2021**, *6*, 2413.
- [6] S.-H. Turren-Cruz, A. Hagfeldt, M. Saliba, *Science* **2018**, *362*, 449.
- [7] Z. Li, M. Yang, J.-S. Park, S.-H. Wei, J. J. Berry, K. Zhu, *Chem. Mater.* **2016**, *28*, 284.
- [8] W. Shockley, H. J. Queisser, *J. Appl. Phys.* **1961**, *32*, 510.
- [9] S. Gholipour, M. Saliba, *Characterization Techniques for Perovskite Solar Cell Materials*, Elsevier, Amsterdam **2020**, pp. 1–22.
- [10] S. Albrecht, M. Saliba, J.-P. Correa-Baena, K. Jäger, L. Korte, A. Hagfeldt, M. Grätzel, B. Rech, *J. Opt.* **2016**, *18*, 064012.
- [11] T. Leijtens, K. A. Bush, R. Prasanna, M. D. McGehee, *Nat. Energy* **2018**, *3*, 828.
- [12] E. T. Hoke, D. J. Slotcavage, E. R. Dohner, A. R. Bowering, H. I. Karunadasa, M. D. McGehee, *Chem. Sci.* **2015**, *6*, 613.
- [13] A. J. Knight, L. M. Herz, *Energy Environ. Sci.* **2020**, *13*, 2024.
- [14] K. Sveinbjörnsson, B. Li, S. Mariotti, E. Jarzembowski, L. Kegelmann, A. Wirtz, F. Frühauf, A. Wehrauch, R. Niemann, L. Korte, F. Fertig, J. W. Müller, S. Albrecht, *ACS Energy Lett.* **2022**, *7*, 2654.
- [15] Y.-H. Lin, N. Sakai, P. Da, J. Wu, H. C. Sansom, A. J. Ramadan, S. Mahesh, J. Liu, R. D. Oliver, J. Lim, L. Aspirtate, K. Sharma, P. K. Madhu, A. B. Morales-Vilches, P. K. Nayak, S. Bai, F. Gao, C. R. M. Grovenor, M. B. Johnston, J. G. Labram, J. R. Durrant, J. M. Ball, B. Wenger, B. Stannowski, H. J. Snaith, *Science* **2020**, *369*, 96.
- [16] L. M. Herz, *Annu. Rev. Phys. Chem.* **2016**, *67*, 65.
- [17] J. Peng, Y. Chen, K. Zheng, T. Pullerits, Z. Liang, *Chem. Soc. Rev.* **2017**, *46*, 5714.
- [18] E. M. Hutter, M. C. Gélvez-Rueda, A. Osherov, V. Bulović, F. C. Grozema, S. D. Stranks, T. J. Savenije, *Nat. Mater.* **2017**, *16*, 115.
- [19] C. M. Wolff, P. Caprioglio, M. Stolterfoht, D. Neher, *Adv. Mater.* **2019**, *31*, 1902762.
- [20] S. G. Motti, D. Meggiolaro, S. Martani, R. Sorrentino, A. J. Barker, F. De Angelis, A. Petrozza, *Adv. Mater.* **2019**, *31*, 1901183.

- [21] A. D. Wright, C. Verdi, R. L. Milot, G. E. Eperon, M. A. Pérez-Osorio, H. J. Snaith, F. Giustino, M. B. Johnston, L. M. Herz, *Nat. Commun.* **2016**, *7*, 11755.
- [22] C. Q. Xia, J. Peng, S. Poncé, J. B. Patel, A. D. Wright, T. W. Crothers, M. Uller Rothmann, J. Borchert, R. L. Milot, H. Kraus, Q. Lin, F. Giustino, L. M. Herz, M. B. Johnston, *J. Phys. Chem. Lett.* **2021**, *12*, 3607.
- [23] M. Baranowski, P. Plochocka, *Adv. Energy Mater.* **2020**, *10*, 1903659.
- [24] L. M. Herz, *J. Phys. Chem. Lett.* **2018**, *9*, 6853.
- [25] A. D. Wright, R. L. Milot, G. E. Eperon, H. J. Snaith, M. B. Johnston, L. M. Herz, *Adv. Funct. Mater.* **2017**, *27*, 1700860.
- [26] Y. Liu, J.-P. Banon, K. Frohna, Y.-H. Chiang, G. Tumen-Ulzii, S. D. Stranks, M. Filoche, R. H. Friend, *ACS Energy Lett.* **2022**, *8*, 250.
- [27] K. Schötz, A. M. Askar, A. Köhler, K. Shankar, F. Panzer, *Adv. Opt. Mater.* **2020**, *8*, 2000455.
- [28] E. M. Hutter, G. E. Eperon, S. D. Stranks, T. J. Savenije, *J. Phys. Chem. Lett.* **2015**, *6*, 3082.
- [29] T. J. Savenije, C. S. Ponceca Jr, L. Kunnehan, M. Abdellah, K. Zheng, Y. Tian, Q. Zhu, S. E. Canton, I. G. Scheblykin, T. Pullerits, A. Yartsev, V. Sundström, *J. Phys. Chem. Lett.* **2014**, *5*, 2189.
- [30] O. G. Reid, M. Yang, N. Kopidakis, K. Zhu, G. Rumbles, *ACS Energy Lett.* **2016**, *1*, 561.
- [31] O. E. Semonin, G. A. Elbaz, D. B. Straus, T. D. Hull, D. W. Paley, A. M. Van der Zande, J. C. Hone, I. Kymissis, C. R. Kagan, X. Roy, J. S. Owen, *J. Phys. Chem. Lett.* **2016**, *7*, 3510.
- [32] R. Meng, G. Wu, J. Zhou, H. Zhou, H. Fang, M. A. Loi, Y. Zhang, *Chem. Eur.* **2019**, *25*, 5480.
- [33] K. J. Savill, M. T. Klug, R. L. Milot, H. J. Snaith, L. M. Herz, *J. Phys. Chem. Lett.* **2019**, *10*, 6038.
- [34] M. J. Trimpl, A. D. Wright, K. Schutt, L. R. Buizza, Z. Wang, M. B. Johnston, H. J. Snaith, P. Müller-Buschbaum, L. M. Herz, *Adv. Funct. Mater.* **2020**, *30*, 2004312.
- [35] S. D. Stranks, V. M. Burlakov, T. Leijtens, J. M. Ball, A. Goriely, H. J. Snaith, *Phys. Rev. Appl.* **2014**, *2*, 034007.
- [36] C. Wehrenfennig, G. E. Eperon, M. B. Johnston, H. J. Snaith, L. M. Herz, *Adv. Mater.* **2014**, *26*, 1584.
- [37] R. Lin, K. Xiao, Z. Qin, Q. Han, C. Zhang, M. Wei, M. I. Saidaminov, Y. Gao, J. Xu, M. Xiao, A. Li, J. Zhu, E. H. Sargent, H. Tan, *Nat. Energy* **2019**, *4*, 864.
- [38] S. Sarkar, V. K. Ravi, S. Banerjee, G. R. Yettapu, G. B. Markad, A. Nag, P. Mandal, *Nano Lett.* **2017**, *17*, 5402.
- [39] G. Xing, N. Mathews, S. Sun, S. S. Lim, Y. M. Lam, M. Grätzel, S. Mhaisalkar, T. C. Sum, *Science* **2013**, *342*, 344.
- [40] Y. Bi, E. M. Hutter, Y. Fang, Q. Dong, J. Huang, T. J. Savenije, *J. Phys. Chem. Lett.* **2016**, *7*, 923.
- [41] A. Kiligaris, P. A. Frantsuzov, A. Yangu, S. Seth, J. Li, Q. An, Y. Vaynzof, I. G. Scheblykin, *Nat. Commun.* **2021**, *12*, 3329.
- [42] A. J. Knight, A. D. Wright, J. B. Patel, D. P. McMeekin, H. J. Snaith, M. B. Johnston, L. M. Herz, *ACS Energy Lett.* **2018**, *4*, 75.
- [43] S. G. Motti, M. Gandini, A. J. Barker, J. M. Ball, A. R. S. Kandada, A. Petrozza, *ACS Energy Lett.* **2016**, *1*, 726.
- [44] T. J. Savenije, D. Guo, V. M. Caselli, E. M. Hutter, *Adv. Energy Mater.* **2020**, *10*, 1903788.
- [45] Y. He, I. Hadar, M. G. Kanatzidis, *Nat. Photonics* **2022**, *16*, 14.
- [46] M. S. Choe, A. Sawant, K.-S. Lee, N. E. Yu, E. Choi, *Appl. Phys. Lett.* **2017**, *110*, 074101.
- [47] M. B. Johnston, L. M. Herz, *Acc. Chem. Res.* **2015**, *49*, 146.
- [48] C. L. Davies, M. R. Filip, J. B. Patel, T. W. Crothers, C. Verdi, A. D. Wright, R. L. Milot, F. Giustino, M. B. Johnston, L. M. Herz, *Nat. Commun.* **2018**, *9*, 293.
- [49] J. M. Richter, M. Abdi-Jalebi, A. Sadhanala, M. Tabachnyk, J. P. Rivett, L. M. Pazos-Outón, K. C. Gödel, M. Price, F. Deschler, R. H. Friend, *Nat. Commun.* **2016**, *7*, 13941.
- [50] A. C. Espenlaub, D. J. Myers, E. C. Young, S. Marcinkevičius, C. Weisbuch, J. S. Speck, *J. Appl. Phys.* **2019**, *126*, 184502.
- [51] A. M. Ulatowski, A. D. Wright, B. Wenger, L. R. Buizza, S. G. Motti, H. J. Eggmann, K. J. Savill, J. Borchert, H. J. Snaith, M. B. Johnston, L. M. Herz, *J. Phys. Chem. Lett.* **2020**, *11*, 3681.
- [52] B. Wu, H. T. Nguyen, Z. Ku, G. Han, D. Giovanni, N. Mathews, H. J. Fan, T. C. Sum, *Adv. Energy Mater.* **2016**, *6*, 1600551.
- [53] D. Meggiolaro, F. De Angelis, *ACS Energy Lett.* **2018**, *3*, 2206.
- [54] W.-J. Yin, T. Shi, Y. Yan, *Appl. Phys. Lett.* **2014**, *104*, 063903.
- [55] T. Leijtens, G. E. Eperon, A. J. Barker, G. Grancini, W. Zhang, J. M. Ball, A. R. S. Kandada, H. J. Snaith, A. Petrozza, *Energy Environ. Sci.* **2016**, *9*, 3472.
- [56] C. S. Ponceca Jr, T. J. Savenije, M. Abdellah, K. Zheng, A. Yartsev, T. Pascher, T. Harlang, P. Chabera, T. Pullerits, A. Stepanov, J.-P. Wolf, V. Sundström, *J. Am. Chem. Soc.* **2014**, *136*, 5189.
- [57] J. Euvrard, O. Gunawan, D. B. Mitzi, *Adv. Energy Mater.* **2019**, *9*, 1902706.
- [58] J. Feng, B. Xiao, *J. Phys. Chem. Lett.* **2014**, *5*, 1278.
- [59] Y. Chang, C. H. Park, K. Matsuishi, *J. Korean Phys. Soc.* **2004**, *44*, 889.
- [60] S. T. A. G. Melissen, F. Labat, P. Sautet, T. Le Bahers, *Phys. Chem. Chem. Phys.* **2015**, *17*, 2199.
- [61] Q. A. Akkerman, S. G. Motti, A. R. Srimath Kandada, E. Mosconi, V. D'Innocenzo, G. Bertoni, S. Marras, B. A. Kamino, L. Miranda, F. De Angelis, A. Petrozza, M. Prato, L. Manna, *J. Am. Chem. Soc.* **2016**, *138*, 1010.
- [62] R. Ahrenkiel, *Solid-State Electron.* **1992**, *35*, 239.
- [63] H.-S. Kim, J.-Y. Seo, N.-G. Park, *ChemSusChem* **2016**, *9*, 2528.
- [64] D. P. McMeekin, G. Sadoughi, W. Rehman, G. E. Eperon, M. Saliba, M. T. Hörantner, A. Haghighirad, N. Sakai, L. Korte, B. Rech, M. B. Johnston, L. M. Herz, H. J. Snaith, *Science* **2016**, *351*, 151.
- [65] National Renewable Energy Laboratory, <https://www.nrel.gov/pv/cell-efficiency.html> (accessed: March 2023).
- [66] A. Al-Ashouri, E. Köhnen, B. Li, A. Magomedov, H. Hempel, P. Caprioglio, J. A. Márquez, A. B. M. Vilches, E. Kasparavicius, J. A. Smith, N. Phung, D. Menzel, M. Grischek, L. Kegelmann, D. Skroblin, C. Gollwitzer, T. Malinauskas, M. Jošt, G. Matic, B. Rech, R. Schlattmann, M. Topic, L. Korte, A. Abate, B. Stannowski, D. Neher, M. Stollerfoht, T. Unold, V. Getautis, S. Albrecht, *Science* **2020**, *370*, 1300.
- [67] E. Zielinski, H. Schweizer, K. Streubel, H. Eisele, G. Weimann, *J. Appl. Phys.* **1986**, *59*, 2196.
- [68] S. Yakunin, L. Protesescu, F. Krieg, M. I. Bodnarchuk, G. Nedelcu, M. Humer, G. De Luca, M. Fiebig, W. Heiss, M. V. Kovalenko, *Nat. Commun.* **2015**, *6*, 8056.
- [69] R. L. Milot, G. E. Eperon, T. Green, H. J. Snaith, M. B. Johnston, L. M. Herz, *J. Phys. Chem. Lett.* **2016**, *7*, 4178.
- [70] V. D'Innocenzo, G. Grancini, M. J. Alcocer, A. R. S. Kandada, S. D. Stranks, M. M. Lee, G. Lanzani, H. J. Snaith, A. Petrozza, *Nat. Commun.* **2014**, *5*, 3586.
- [71] R. L. Milot, G. E. Eperon, H. J. Snaith, M. B. Johnston, L. M. Herz, *Adv. Funct. Mater.* **2015**, *25*, 6218.
- [72] A. Biewald, N. Giesbrecht, T. Bein, P. Docampo, A. Hartschuh, R. Ciesielski, *ACS Appl. Mater. Interfaces* **2019**, *11*, 20838.
- [73] J. M. Frost, *Phys. Rev. B* **2017**, *96*, 195202.
- [74] S. Poncé, M. Schlipf, F. Giustino, *ACS Energy Lett.* **2019**, *4*, 456.
- [75] R. L. Milot, M. T. Klug, C. L. Davies, Z. Wang, H. Kraus, H. J. Snaith, M. B. Johnston, L. M. Herz, *Adv. Mater.* **2018**, *30*, 1804506.
- [76] C. L. Davies, J. Borchert, C. Q. Xia, R. L. Milot, H. Kraus, M. B. Johnston, L. M. Herz, *J. Phys. Chem. Lett.* **2018**, *9*, 4502.
- [77] C. Wehrenfennig, M. Liu, H. J. Snaith, M. B. Johnston, L. M. Herz, *Energy Environ. Sci.* **2014**, *7*, 2269.
- [78] M. B. Johnston, L. M. Herz, *Acc. Chem. Res.* **2016**, *49*, 146.
- [79] T. S. Sarker, C. Momblona, L. Gil-Escrig, J. Avila, M. Sessolo, H. J. Bolink, L. J. A. Koster, *ACS Energy Lett.* **2017**, *2*, 1214.

- [80] M. M. Lee, J. Teuscher, T. Miyasaka, T. N. Murakami, H. J. Snaith, *Science* **2012**, 338, 643.
- [81] H.-S. Kim, C.-R. Lee, J.-H. Im, K.-B. Lee, T. Moehl, A. Marchioro, S.-J. Moon, R. Humphry-Baker, J.-H. Yum, J. E. Moser, M. Grätzel, N.-G. Park, *Sci. Rep.* **2012**, 2, 591.
- [82] J. Jeong, M. Kim, J. Seo, H. Lu, P. Ahlawat, A. Mishra, Y. Yang, M. A. Hope, F. T. Eickemeyer, M. Kim, Y. J. Yoon, I. W. Choi, B. P. Darwich, S. J. Choi, Y. Jo, J. H. Lee, B. Walker, S. M. Zakeeruddin, L. Emsley, U. Rothlisberger, A. Hagfeldt, D. S. Kim, M. Grätzel, J. Y. Kim, *Nature* **2021**, 592, 381.
- [83] N. Onoda-Yamamuro, T. Matsuo, H. Suga, *J. Phys. Chem. Solids* **1992**, 53, 935.
- [84] G. Schuck, D. M. Töbrens, M. Koch-Müller, I. Efthimiopoulos, S. Schorr, *J. Phys. Chem. C* **2018**, 122, 5227.
- [85] A. Osherov, E. M. Hutter, K. Galkowski, R. Brenes, D. K. Maude, R. J. Nicholas, P. Plochocka, V. Bulović, T. J. Savenije, S. D. Stranks, *Adv. Mater.* **2016**, 28, 10757.
- [86] C. Wehrenfennig, M. Liu, H. J. Snaith, M. B. Johnston, L. M. Herz, *APL Mater.* **2014**, 2, 081513.
- [87] T. Kirchartz, T. Markvart, U. Rau, D. A. Egger, *J. Phys. Chem. Lett.* **2018**, 9, 939.
- [88] F. Staub, U. Rau, T. Kirchartz, *ACS Omega* **2018**, 3, 8009.
- [89] R. Elliott, *Phys. Rev.* **1957**, 108, 1384.
- [90] K. Xiao, J. Wen, Q. Han, R. Lin, Y. Gao, S. Gu, Y. Zang, Y. Nie, J. Zhu, J. Xu, H. Tan, *ACS Energy Lett.* **2020**, 5, 2819.
- [91] R. J. Sutton, G. E. Eperon, L. Miranda, E. S. Parrott, B. A. Kamino, J. B. Patel, M. T. Hörantner, M. B. Johnston, A. A. Haghighirad, D. T. Moore, H. J. Snaith, *Adv. Energy Mater.* **2016**, 6, 1502458.
- [92] S. Ullah, J. Wang, P. Yang, L. Liu, S.-E. Yang, T. Xia, H. Guo, Y. Chen, *Mater. Adv.* **2021**, 2, 646.
- [93] J. Li, R. Gao, F. Gao, J. Lei, H. Wang, X. Wu, J. Li, H. Liu, X. Hua, S. F. Liu, *J. Alloys Compd.* **2020**, 818, 152903.
- [94] G. Tong, T. Chen, H. Li, L. Qiu, Z. Liu, Y. Dang, W. Song, L. K. Ono, Y. Jiang, Y. Qi, *Nano Energy* **2019**, 65, 104015.
- [95] G. Williams, D. C. Watts, *Trans. Faraday Soc.* **1970**, 66, 80.
- [96] F. Alvarez, A. Alegria, J. Colmenero, *Phys. Rev. B* **1991**, 44, 7306.
- [97] J. Fu, N. F. Jamaludin, B. Wu, M. Li, A. Solanki, Y. F. Ng, S. Mhaisalkar, C. H. A. Huan, T. C. Sum, *Adv. Energy Mater.* **2019**, 9, 1803119.
- [98] G. Xing, N. Mathews, S. S. Lim, N. Yantara, X. Liu, D. Sabba, M. Grätzel, S. Mhaisalkar, T. C. Sum, *Nat. Mater.* **2014**, 13, 476.
- [99] H.-H. Fang, R. Raissa, M. Abdu-Aguye, S. Adjokatse, G. R. Blake, J. Even, M. A. Loi, *Adv. Funct. Mater.* **2015**, 25, 2378.
- [100] W. Kong, Z. Ye, Z. Qi, B. Zhang, M. Wang, A. Rahimi-Iman, H. Wu, *Phys. Chem. Chem. Phys.* **2015**, 17, 16405.
- [101] N. Sestu, M. Cadelano, V. Sarritzu, F. Chen, D. Marongiu, R. Piras, M. Mainas, F. Quochi, M. Saba, A. Mura, G. Bongiovanni, *J. Phys. Chem. Lett.* **2015**, 6, 4566.
- [102] K. Galkowski, A. Mitioglu, A. Miyata, P. Plochocka, O. Portugall, G. E. Eperon, J. T.-W. Wang, T. Stergiopoulos, S. D. Stranks, H. J. Snaith, L. M. Herz, M. B. Johnston, *Energy Environ. Sci.* **2016**, 9, 962.
- [103] N. K. Noel, S. N. Habisreutinger, B. Wenger, M. T. Klug, M. T. Hörantner, M. B. Johnston, R. J. Nicholas, D. T. Moore, H. J. Snaith, *Energy Environ. Sci.* **2017**, 10, 145.
- [104] J. B. Patel, A. D. Wright, K. B. Lohmann, K. Peng, C. Q. Xia, J. M. Ball, N. K. Noel, T. W. Crothers, J. Wong-Leung, H. J. Snaith, L. M. Herz, M. B. Johnston, *Adv. Energy Mater.* **2020**, 10, 1903653.
- [105] A. M. Ulatowski, M. D. Farrar, H. J. Snaith, M. B. Johnston, L. M. Herz, *ACS Photonics* **2021**, 8, 2509.
- [106] P. Tiwana, P. Parkinson, M. B. Johnston, H. J. Snaith, L. M. Herz, *J. Phys. Chem. C* **2010**, 114, 1365.
- [107] T. Seifert, S. Jaiswal, U. Martens, J. Hannegan, L. Braun, P. Maldonado, F. Freimuth, A. Kronenberg, J. Henrizi, I. Radu, E. Beaurepaire, Y. Mokrousov, P. M. Oppeneer, M. Jourdan, G. Jakob, D. Turchinovich, L. M. Hayden, M. Wolf, M. Münzenberg, M. Kläui, T. Kampfrath, *Nat. Photonics* **2016**, 10, 483.
- [108] L. R. Buizza, H. C. Sansom, A. D. Wright, A. M. Ulatowski, M. B. Johnston, H. J. Snaith, L. M. Herz, *Adv. Funct. Mater.* **2022**, 32, 2108392.
- [109] M. Tinkham, *Phys. Rev.* **1956**, 104, 845.
- [110] C. L. Davies, J. B. Patel, C. Q. Xia, L. M. Herz, M. B. Johnston, *J. Infrared, Millimeter, Terahertz Waves* **2018**, 39, 1236.
- [111] H. Hempel, T. J. Savenije, M. Stolterfoht, J. Neu, M. Failla, V. C. Paingad, P. Kužel, E. J. Heilweil, J. A. Spies, M. Schleuning, J. Zhao, D. Friedrich, K. Schwarzburg, L. D. A. Siebbeles, P. Dörflinger, V. Dyakonov, R. Katoh, M. J. Hong, J. G. Labram, M. Monti, E. Butler-Caddle, J. Lloyd-Hughes, M. M. Taheri, J. B. Baxter, T. J. Magnanelli, S. Luo, J. M. Cardon, S. Ardo, T. Unold, *Adv. Energy Mater.* **2022**, 12, 2102776.